

Disk vs wind accretion in X-ray pulsar GX 301-2

Jiren Liu^{1*}, Long Ji^{2,7}, Peter A. Jenke³, Victor Doroshenko², Zhenxuan Liao⁴, Xiaobo Li⁵, Shuangnan Zhang⁵, Mauro Orlandini⁶, Mingyu Ge⁵, Shu Zhang⁵, Andrea Santangelo²

¹Beijing Planetarium, Xizhimenwai Road, Beijing 100044, China

²Institut für Astronomie und Astrophysik, Kepler Center for Astro and Particle Physics, Eberhard Karls Universität, Sand 1, 72076 Tübingen, Germany

³University of Alabama in Huntsville, Huntsville, AL 35812, USA

⁴National Astronomical Observatories, 20A Datun Road, Beijing 100012, China

⁵Key Laboratory for Particle Astrophysics, Institute of High Energy Physics, Beijing 100049, China

⁶INAF Osservatorio di Astrofisica e Scienza dello Spazio di Bologna, Via Piero Gobetti 101, I-40129 Bologna, Italy

⁷School of physics and astronomy, Sun Yat-Sen University, Zhuhai, Guangdong 519082, China

ABSTRACT

GX 301-2 provides a rare opportunity to study both disk and wind accretion in a same target. We report *Insight-HXMT* observations of the spin-up event of GX 301-2 happened in 2019 and compare with those of wind-fed state. The pulse profiles of the initial rapid spin-up period are dominated by one main peak, while those of the later slow spin-up period are composed of two similar peaks, as those of wind-fed state. These behaviors are confirmed by *Fermi*/GBM data, which also show that during the rapid spin-up period, the main peak increases with luminosity up to 8×10^{37} erg s⁻¹, but the faint peak keeps almost constant. The absorption column densities during the spin-up period are $\sim 1.5 \times 10^{23}$ cm⁻², much less than those of wind-fed state at similar luminosity ($\sim 9 \times 10^{23}$ cm⁻²), supporting the scenario that most of material is condensed into a disk during the spin-up period. We discuss possible differences between disk and wind accretion that may explain the observed different trend of pulse profiles.

Key words: Accretion –pulsars: individual: GX 301-2 – X-rays: binaries

1 INTRODUCTION

X-ray pulsars are powered by accretion of material from a normal companion star onto a rotating magnetized neutron star. The mass transfer process could be through either a stellar wind or a Roche-Lobe overflow (RLOF). For RLOF, the transferred material has sufficient angular momentum to form a rotating disk, through which the matter spirals towards the neutron star (Pringle & Rees 1972). On the other hand, the transfer of stellar wind resembles Bondi-Hoyle accretion with a quasi-spherical distribution (Davidson & Ostriker 1973), although formation of short-lived transient accretion disks is also possible (Fryxell & Taam 1988; Blondin & Pope 2009; Xu & Stone 2019). The disk accretion transfers angular momentum to the neutron star and leads to variations of spin frequency of the neutron star measurable on days timescale, while wind accretion results in stochastic spin-frequency changes on

shorter timescales. Both the disk and wind flow will be dominated by the magnetic field within the magnetosphere and will be channeled along the magnetic field lines to the surface of the neutron star (e.g. Davidson 1973; Basko & Sunyaev 1976).

Generally, mass transfer in X-ray pulsars is dominated by one of mechanisms, either wind or disk accretion, but there are a few X-ray pulsars showing both wind and disk accretion alternately. These sources are ideal targets to study the differences between different accretion processes, since the major parameters of the system, such as the magnetic field and inclination angle, are not changed. The classical wind-fed X-ray pulsar, GX 301-2, is such a source.

GX 301-2 is a slow rotator with a pulse period ~ 680 s (White et al. 1971), an orbital period ~ 41.5 days and an orbital eccentricity ~ 0.46 (Sato et al. 1986; Koh et al. 1997). Its optical companion, Wray 977, has a mass of $39 - 53M_{\odot}$ and a radius of $62R_{\odot}$, close to the Roche lobe radius near periastron (Kaper et al. 2006). Its spin history monitored by BATSE on *Compton* observatory and GBM on *Fermi*

* E-mail: liujiren@bjp.org.cn

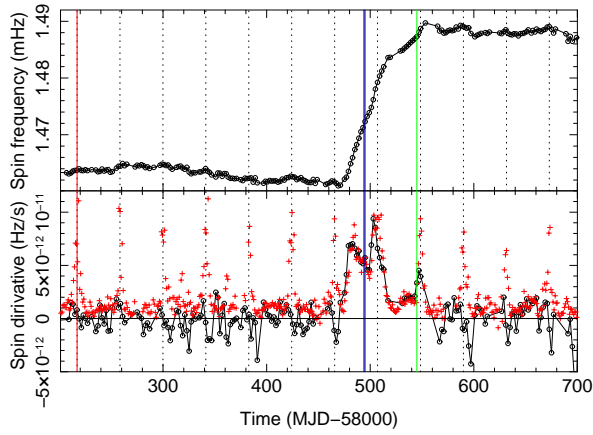


Figure 1. The 2019 spin-up event of GX 301-2 monitored by *Fermi*/GBM (top panel), together with the spin derivatives (circles in bottom panel). The corresponding *Swift*/BAT 15-50 keV fluxes (multiplied by a factor of 5×10^{-11} , red pluses) are over-plotted. Vertical dotted lines indicate the time of periastron, and vertical solid lines indicate dates of *HXMT* observations analyzed.

spacecraft is composed of long period of small frequency variability and several rapid spin-up events lasting for tens of days (Koh et al. 1997). The long periods of small stochastic spin frequency changes indicate wind accretion, while the spin-up events implies transient disk accretion. Indeed, during the spin-up events, its spin derivatives were found to be correlated with fluxes ($\dot{\nu} \propto F^{0.75 \pm 0.05}$), consistent with a scenario of disk accretion (Liu 2020). There may be also some correlations between fluxes and spin derivatives during wind state (Doroshenko et al. 2010).

A strong spin-up event of GX 301-2 happened between Dec. 2018 and Mar. 2019. Nabizadeh et al. (2019) reported *NuSTAR* observations of GX 301-2 near the end of this spin-up event (Mar. 3, 2019, MJD 58545) and found no significant differences in spectral and temporal properties compared with normal wind-fed state. In contrast, with X-Calibur polarimeter, *NICER*, and *Swift* observations of GX 301-2 during the initial spin-up period (around Dec. 31, 2018, MJD 58483), Abarr et al. (2020) found that its pulse profiles are strongly dominated by one main peak, quite different from two approximately equal peaks in normal wind-fed state. In this paper we analyze Insight Hard X-ray Modulation Telescope (*HXMT*) observations of GX 301-2 during the spin-up episode performed around Jan. 11-12, 2019, i.e. right in the middle of this event with the aim to study the differences between wind and disk accretion of GX 301-2.

2 OBSERVATION DATA

Insight-HXMT is a Chinese X-ray satellite launched on June, 2017. It carries three collimated instruments sensitive to different energy bands: low energy telescope (LE, 1-15 keV), medium energy telescope (ME, 5-30 keV), and high energy telescope (HE, 20-250 keV). The corresponding effective areas are 384, 952, and 5100 cm², respectively. For details of *HXMT* we refer to Zhang et al. (2020) and references therein. The Gamma-ray Burst Monitor (GBM,

Table 1. List of *HXMT* observations

ObsID	t_{exp} (ks)	Obs date	MJD	note
P0101309019	1.6	2019-01-11	58494	rapid spin-up (D)
P0101309020	2.9	2019-01-12	58495	rapid spin-up (D)
P0101309021	14.2	2019-03-03	58545	slow spin-up (SD)
P0101309015	10.2	2018-04-09	58217	wind state (W)

Note: t_{exp} refers to the effective exposure of the ME telescope.

Meegan et al. 2009) on the *Fermi* spacecraft is continuously monitoring the spin histories of X-ray pulsars¹ (Finger et al. 2009; Malacaria et al. 2020).

Fermi/GBM detected one strong spin-up event of GX 301-2 around Jan., 2019, which is presented in Figure 1. The spin-up event started around an orbital phase 0.22 (Dec. 23, 2018, MJD 58475) and reached a rapid spin-up rate $\sim 6 \times 10^{-12}$ Hz/s. The spin-up rate was further increased a little bit ($\sim 1 \times 10^{-11}$ Hz/s) just prior to periastron. After periastron, the spin-up rate slowed down to about 2×10^{-12} Hz/s, and then increased to $\sim 4 \times 10^{-12}$ Hz/s near the second periastron. After the second periastron, the spin-up event ended. Good correspondence between the spin-up rates and the *Swift*/BAT fluxes can be seen during the spin-up episode (see Liu 2020, for more details).

HXMT observed GX 301-2 twice during the initial rapid spin-up period on Jan. 11 and 12, 2019 (MJD 58494 and 58495), and once during the later slow spin-up phase (Mar. 3, 2019, MJD 58545). The later observation was taken on the same day with *NuSTAR* discussed by Nabizadeh et al. (2019). These *HXMT* observations are complementary to X-Calibur, *Swift*/XRT, and *NICER* observations reported previously, since *HXMT* provides simultaneous broad band data during the middle of the rapid spin-up period. For comparison, we also analyzed other *HXMT* observations of GX 301-2 before the 2019 spin-up event. The observation details are listed in Table 1. The data are processed using *HXMT*-DAS2.03 following the analysis guide. Both barycentric and binary orbital corrections are applied to the light curves, and the ephemeris parameters from Doroshenko et al. (2010) are adopted.

3 TIMING ANALYSIS

To study the energy dependences of the pulse profile, we adopted four energy bands: 2-7, 8-15, 15-30, and 30-50 keV. The photons within 2-7 keV are from LE detectors, 8-30 keV from ME detectors, and 30-50 keV from HE detectors. We extracted the pulse profiles of different energies from initial rapid spin-up periods, MJD 58494 and 58495, which we refer as "D" (disk state). To compare with those observed during the wind-fed state, we also extracted the pulse profiles from the observation taken on MJD 58217, when the source was observed during the so-called pre-periastron flare at flux level comparable to that during the rapid spin-up episode. At this time the spin evolution observed by GBM indicates no apparent spin-up trend and we refer as "W" (wind state). We also extracted the profiles from the observation on MJD

¹ <https://gammaray.msfc.nasa.gov/gbm/science/pulsars/>

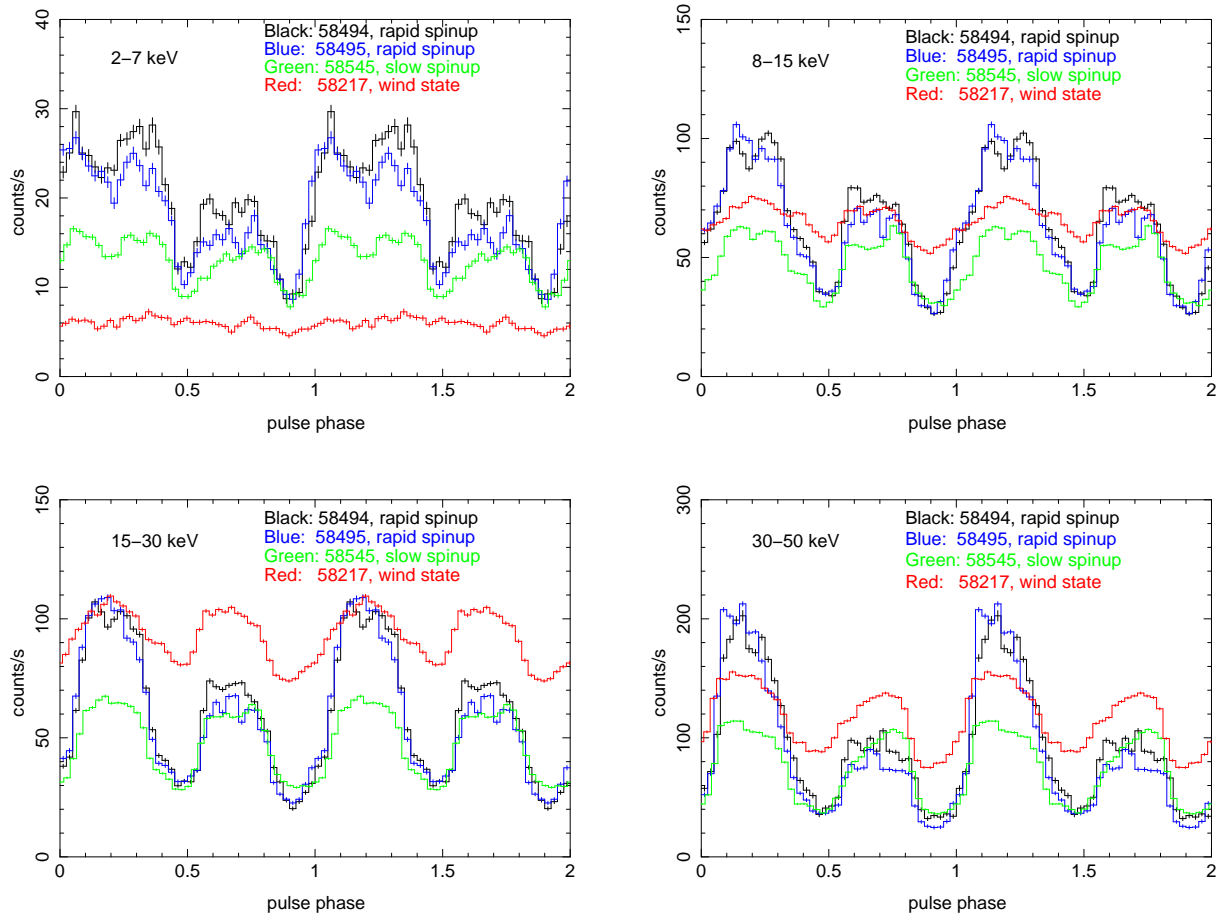


Figure 2. Pulse profiles of GX 301-2 observed by *HXMT* around MJD 58494, 59495, 58545 and 58217 at four different energy bands. The profiles of the rapid spin-up period (MJD 58494 and 59495) are dominated by one main peak, while others are composed of two similar peaks. MJD 58217 represents a typical wind-fed state with a flux similar to those of the rapid spin-up period (MJD 58494 and 59495).

58545, which is referred as "SD" (slow spin-up state). The pulse periods are calculated from the spin measurement by *Fermi*/GBM. While the phase of MJD 58494 and 58495 are calculated assuming a constant spin-up rate, those of MJD 58217 and 58545 are shifted to match the profiles of MJD 58494 and 58495. The extracted pulse profiles for all four energy bands and four observations are presented in Figure 2.

As can be seen, most of the profiles within one spin period are composed of two peaks, which are separated by half period. During the rapid spin-up periods (MJD 58494-58495, D) one of the peaks of the pulse profile is significantly higher than the other one, and we refer the higher peak as main peak (phase -0.08-0.42) and the fainter one as faint peak (phase 0.42-0.92). We define the peak fluence as the pulsed flux integrated over time, and the pulsed flux means the flux minus the minimum flux during the whole spin period. The fluence ratio between the main and faint peaks (f_{MF}) is about 1.6 for photons within 8-30 keV for MJD 58494 and is about 2.0 for MJD 58495. This behavior is similar to X-Calibur result observed around MJD 58483 (Abarr et al. 2020). For 30-50 keV, the main-to-faint contrast is higher, and f_{MF} is 2.3 for MJD 58494 and 2.8 for MJD 58495.

In contrast, the profiles of the slow spin-up period (MJD 58545, SD) show two similar peaks, similar to the *NuSTAR* results observed on the same day (Nabizadeh et al. 2019). The corresponding f_{MF} of MJD 58545 are about 1.2-1.3 for photons within 8-30 keV and has a similar value within 30-50 keV. We note that for photons above 15 keV, the higher fluence ratio of MJD 58494 and 58495 (D) are mainly due to the higher fluxes of the main peak. That is, the fluxes of the main peak of the rapid spin-up periods increase significantly compared with those of the slow spin-up period, while the fluxes of the faint peak do not increase that much.

For the wind-fed state (MJD 58217, W), the two peaks have similar fluxes for all energies, except for the lowest energies (2-7 keV), where the pulse profile becomes flat. The corresponding f_{MF} of MJD 58217 are about 1.2-1.3 for photons within both 8-30 keV and 30-50 keV, similar to those of the slow spin-up period. The pulse fraction (defined as $\frac{f_{max}-f_{min}}{f_{max}+f_{min}}$) of the wind-fed state is apparently smaller than those of the spin-up periods. While the fluxes of the wind-fed state (MJD 58217) is similar to those of MJD 58494 and 58495 (D) for energies within 8-15 keV and 30-50 keV, they are higher than those of MJD 58494 and 58495 within 15-30

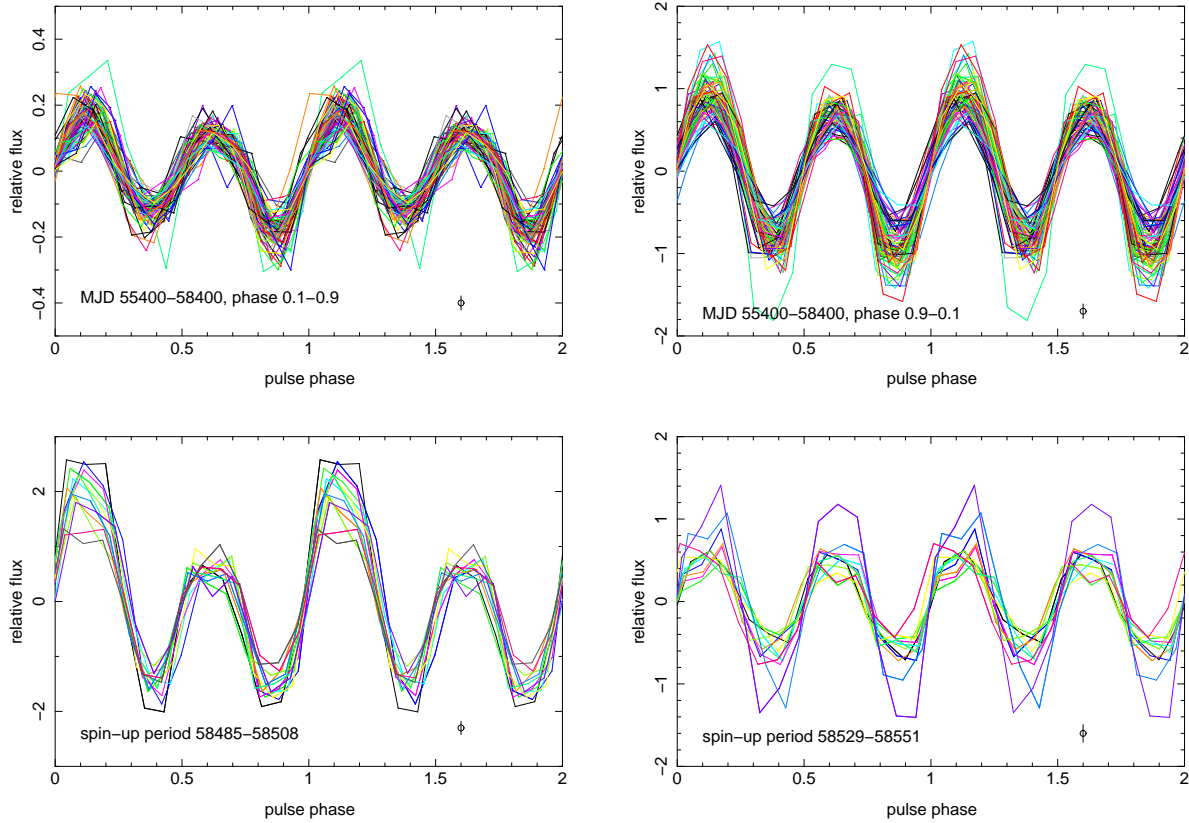


Figure 3. 12-25 keV pulse profile of GX 301-2 extracted from *Fermi*/GBM data during non spin-up periods and 2019 spin-up episode. The non spin-up periods are divided into orbital phase intervals of 0.1-0.9 and 0.9-0.1, while the spin-up episode is divided into initial rapid spin-up and later slow spin-up phase. The inset circles represent mean errors of the relative fluxes. Different colors correspond to measurements at different intervals.

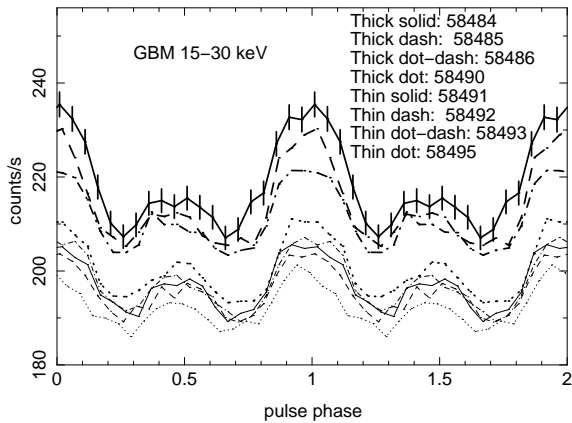


Figure 4. 15-30 keV pulse profile of GX 301-2 extracted from *Fermi*/GBM data based on individual daily extractions. For clarity, only the errors of MJD 58484 are plotted.

keV, as shown by the apparent higher faint peak of the wind state.

Another feature of the pulse profiles observed during the spin-up period is that the lower the energy, the broader the main peak width. The plateau of the 2-7 keV main peak occupies almost half spin period, and it seems to be com-

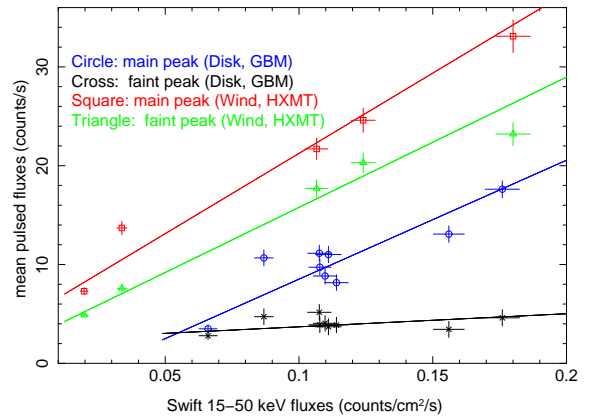


Figure 5. 15-30 keV mean pulsed fluxes of the main and faint peaks plotted against the *Swift* daily 15-50 keV fluxes for disk (extracted from *Fermi*/GBM) and wind (extracted from *HXMT*) state. The solid lines are linear fits to the data. The two data points of disk state around 0.06-0.07 are the *HXMT* results on MJD 58545 (SD) extrapolated to *Fermi*/GBM values.

posed of two separate spikes. There are also two spikes in the main peaks of 8-15, but is not as apparent as those of the 2-7 keV main peak.

Considering that the effective exposure of *HXMT* observations of the spin-up event of GX 301-2 lasts only a few ks, and thus only includes a few pulse cycles and can be biased by stochastic variations, we also investigated pulse profile evolution using *Fermi*/GBM data. As *Fermi*/GBM data is dominated by the background, the constant component of the light curve is subtracted and only the pulsed profile is obtained (e.g. Finger et al. 2009). Since the orbital light curves of GX 301-2 show flares near periastron, for non spin-up periods (MJD 55400-58400, 3000 days in total) we divided the orbital phase into two intervals of 0.1-0.9 and 0.9-0.1. There are three continuous data type for GBM: CTIME data with 8 energy channels and 0.256 s time bin, CSPEC data with 128 channels and 4.096 s bin, and CTTE photon events data. *Fermi*/GBM made a measurement of pulse profile and spin period of GX 301-2 for every ~ 2 days interval using CTIME data. All the 12-25 keV profiles within the corresponding periods are presented in Figure 3, with different colors indicating measurements at different intervals.

As can be seen, the pulse profiles outside of the spin-up periods show two similar peaks, although with different pulsed amplitude for phase intervals of 0.1-0.9 and 0.9-0.1. The main-to-faint fluence ratios are around 1.2-1.3 estimated from the pulsed fluxes. For the 2019 spin-up event, the main peaks during the initial rapid spin-up period (MJD 58485-58508) are much higher than the faint peaks, similar to the *HXMT* results around MJD 58494 and 58495. While those during the slow spin-up period (MJD 58529-58551) show two similar peaks, similar to the *HXMT* and *NuSTAR* results on MJD 58545.

The high fluxes of GX 301-2 during the initial rapid spin-up period also allow us to extract background unsubtracted individual pulse profiles of GX 301-2 from the *Fermi*/GBM data, and to study the temporal behavior at fluxes higher than those of *HXMT* observations. We used GBM CSPEC data from N0 detector, which has the best viewing angle for GX 301-2 during these time. The time periods are picked up by eyes to have clear pulsations around 680 s, and the effective area is required to be larger than 80% of the maximum value during that day. The extracted 15-30 keV profiles on date Jan. 1, 2, 3, 7, 8, 9, 10, and 12 are plotted in Figure 4. As can be seen, the fluence of the main peak decrease with the increasing date, while the fluence of the faint peak show less changes. In Figure 5, we plot the GBM mean pulsed fluxes of the main and faint peaks vs the daily *Swift*/BAT 15-50 keV fluxes. It shows clearly that the main peak fluxes increase with the *Swift* fluxes, while the faint peak fluxes not. The fluence ratio f_{MF} is about 4 for the largest fluxes on MJD 58484.

To check the behavior of pulse profile of wind-fed state with luminosity, we also analyzed *HXMT* observations of GX 301-2 with good signal and good pulse detection. These observations are on MJD 57968, 57969, 58121, 58138, 58148, and 58217. The measured mean pulsed fluxes of the main and faint peaks are over-plotted in Figure 5. The uncertainties of these measurements are dominated by flux variations of GX 301-2 on time scale of hours for wind-fed state, which are hard to estimate due to the limited *HXMT* effective exposures. Nevertheless, the main-to-faint ratios are generally much stable, and we have assumed %5 uncertainties of the measured fluxes. Both fluxes of the main and faint peaks in-

crease with luminosity for wind-fed state, and no significant increase of the main-to-faint ratio is found for the observed luminosity.

4 SPECTRAL ANALYSIS

As illustrated in Figure 2, the pulse profiles during the spin-up episode are energy dependent. To study the energy spectrum of the main and faint peaks, we extracted the spectrum of the main and faint peaks from both MJD 58494 and 58495 (D) observations, separately. They are plotted in the top panel of Figure 6. To help the comparison, the spectra of faint peaks are multiplied by a factor to make the fluxes of faint peaks around 15 keV similar to those of main peaks. The spectra of main peaks and normalized faint peaks are quite similar, although show a slightly different curvature, for both MJD 58494 and 58495.

To model the observed spectra, following Kreykenbohm et al. (2004), we fit an absorbed power-law model with a Fermi-Dirac cutoff (Tanaka 1986): $1/\{\exp[(E - E_{cut})/E_{fold}] + 1\}$, where E_{cut} and E_{fold} are the cutoff and folding energy. We add a Gaussian absorption line around 30-35 keV to model the CRSF. We also add a Gaussian emission line around 6.4 keV to represent the Fe $K\alpha$ line, and its width is fixed as 0.01 keV. The low energy absorption is modelled with *tbabs* (Wilms et al. 2000). Thus, the adopted model is as follows:

$$F(E) = FDcut * Gabs * tbabs * powerlaw + gauss. \quad (1)$$

The fitting results are plotted in Figure 6 and listed in Table 2. The absorption-corrected luminosities within 1-50 keV, assuming a distance of 3.5 kpc (Nabizadeh et al. 2019), are also listed.

As can be seen, the model provides a reasonable fit to the observed spectra. From Table 2 we see that the most apparent difference between the main and faint peaks is the normalizations of the power-law model. The differences of fitted cutoff energy and folding energy between the main and faint peaks explain their spectral differences above 30 keV. The absorption column densities of the faint peaks are a little larger than that of the main peak, which explain the relatively lower continua of the faint peaks at low energy. We note that the differences of absorption between different peaks can not be due to variations far away from GX 301-2, but should originate in vicinity of the neutron star. While the inclusion of CRSF model improves the fitting results, some CRSF parameters are not well constrained and are fixed as values of the other peak.

On the other hand, the fluxes of the Fe $K\alpha$ line are similar between the main and faint peaks for both MJD 58494 and 58495. It implies that the illumination of the Fe $K\alpha$ -emitting gas is similar during the main and faint peaks. This could be obtained if the Fe $K\alpha$ -emitting gas is quasi-symmetric with respect to the rotation direction of the neutron star.

The spectra of the main and faint peaks of the slow spin-up period (MJD 58545, SD) are plotted in the bottom left panel of Figure 6. They show similar behaviors as those of MJD 58494 and 58495 (D). The fitting residuals around 10 keV is large for MJD 58545 (SD). Such residuals could be due to instrument. Because different temperatures of ME

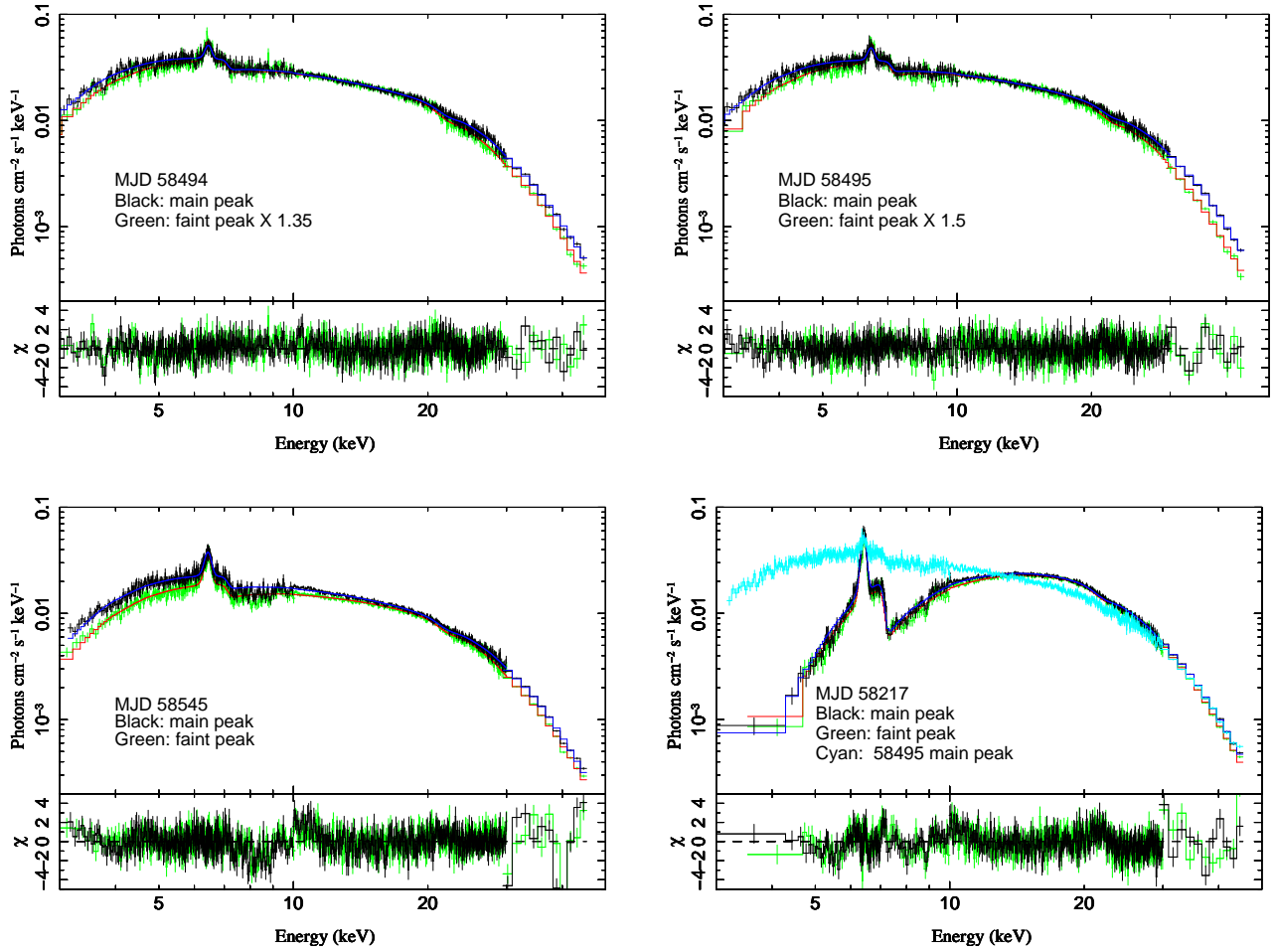


Figure 6. *HXMT* broadband spectra of the main and faint peaks during the rapid spin-up period MJD 58494 and 58495, the slow spin-up period MJD 58545, and the wind-fed state MJD 58217. For comparison, the spectra of faint peaks of MJD 58494 and 58495 are multiplied by a factor to make their fluxes similar as the main peaks around 15 keV.

Table 2. Fitting results of the model of Eq. 1

Peak	N_H 10^{22} cm^{-2}	A(PL)	Γ (PL)	E_{cut} keV	E_{fold} keV	E_{cyc}	σ_{cyc} keV	D_{cyc} keV	Norm(Fe)	$\chi^2_{\nu}(dof)$	$L_{1-50keV}$ 10^{37} erg/s
58494 main	15.1 ± 0.7	0.24 ± 0.03	0.83 ± 0.05	26.9 ± 1.0	5.9 ± 0.3	32.7 ± 1.9	4.4 ± 1.5	2.2 ± 1.5	3.5 ± 0.6	0.98 (548)	4.4
58494 faint	15.9 ± 1.0	0.14 ± 0.02	0.70 ± 0.06	23.6 ± 1.0	5.8 ± 0.2	30.8 ± 3.4	3.8 ± 2.3	1.3 ± 1.3	4.1 ± 0.5	0.99 (456)	2.4
58495 main	15.3 ± 0.7	0.22 ± 0.02	0.79 ± 0.04	26.3 ± 0.8	5.8 ± 0.2	32.1 ± 2.0	3.3 ± 2.2	0.8 ± 0.8	3.2 ± 0.6	0.92 (573)	4.1
58495 faint	17.6 ± 1.3	0.12 ± 0.02	0.72 ± 0.07	23.7 ± 0.8	5.4 ± 0.1	32.1	3.3	0.9 ± 0.5	3.4 ± 0.5	1.10 (400)	2.2
58545 main	18.5 ± 0.7	0.13 ± 0.01	0.77 ± 0.05	26.3 ± 0.9	5.9 ± 0.1	32	4.9 ± 1.0	1.3 ± 0.8	4.5 ± 0.3	1.41 (640)	2.7
58545 faint	19.5 ± 1.0	0.09 ± 0.01	0.63 ± 0.05	25.4 ± 1.0	5.6 ± 0.2	32.0 ± 0.9	4.6 ± 1.1	2.6 ± 1.3	4.7 ± 0.3	1.16 (578)	2.2
58217 main	87 ± 5	0.28 ± 0.09	0.72 ± 0.12	24.3 ± 1.5	5.5 ± 0.2	32.5 ± 1.0	5.8 ± 1.1	3.0 ± 1.9	9.4 ± 0.4	1.28 (483)	5.1
58217 faint	84 ± 5	0.17 ± 0.05	0.54 ± 0.12	23.6 ± 1.1	5.2 ± 0.1	32.2 ± 1.0	5.8	3.0 ± 0.6	9.0 ± 0.4	1.46 (468)	4.3

Note: A(PL) is in units of photons $\text{keV}^{-1} \text{cm}^{-2} \text{s}^{-1}$ at 1 keV, Norm(Fe) is in units of 10^{-3} photons $\text{cm}^{-2} \text{s}^{-1}$, and some CRSF energies and widths are not well constrained and they are fixed as those of the other peak.

detectors could affect the response of low energy part and are not modeled in current version of data reduction pipeline, we have used LE data for 8-10 keV. The 10-11 keV band of ME could still be affected. On the other hand, the particle background of LE starts to become significant around 7-10 keV (Liao et al. 2020). These two instrument effects could lead to the residual around 10 keV of MJD 58545 (SD),

when the fluxes is lower than those of MJD 58494-58495 (D). Although with these caveats, the spectral shape of MJD 58545 (SD) is quite similar to those of MJD 58494 and 58495 (D).

The spectra of wind-fed state observation (MJD 58217, W) are plotted in the bottom right panel of Figure 6. For comparison, the main peak spectrum of MJD 58495 (D) is

over-plotted. As can be seen, the spectra of the two peaks of MJD 58217 are quite similar. They are also similar to that of the main peak of MJD 58495 above 30 keV. The 6.4 keV Fe K α line of MJD 58217 is very prominent, together with a sharp absorption edge around 7 keV. These spectral features of MJD 58217 are typical of Compton reprocessed emission from neutral-like gas. We also fit the wind-fed state spectra with the model of Eq.1, and the results are plotted with the observed spectra and listed in Table 2. The best-fitted absorption column densities are around $8.5 \times 10^{23} \text{ cm}^{-2}$, much larger than those of the spin-up period. The equivalent widths (EW) of the Fe K α line are about 0.7 keV, also much larger than those of the spin-up period (~ 0.15 keV). The residuals around 7 keV are the Fe K β line, which is not modeled in Eq. 1. The residuals around 23 keV could be due to phase-dependent features of high energy cutoff (e.g. Fürst et al. 2018), and here the phases are only divided into main and faint peaks. The residuals around 10 keV could be due to instrument as discussed above. It is interesting to note that 10 keV bumps have been observed on the spectrum of many X-ray pulsars (e.g. Coburn et al. 2002) and could be due to imperfect model of the continuum of X-ray pulsars.

5 DISCUSSION AND CONCLUSION

We studied the temporal and spectral differences of GX 301-2 between the spin-up state and the wind-fed non spin-up state. During the initial rapid spin-up period of the 2019 spin-up event of GX 301-2, the main peak is higher than the faint peak. During the late slow spin-up period, the pulse profiles are composed of two similar peaks, similar to those of wind-fed state. The line-of-sight absorption column densities are about $1.5 \times 10^{23} \text{ cm}^{-2}$ for spin-up periods, and $\sim 9 \times 10^{23} \text{ cm}^{-2}$ for wind-fed state of similar fluxes. The EWs of Fe K α line are about 0.15 keV for spin-up periods, and ~ 0.7 keV for wind-fed state of similar fluxes.

For wind accretion, after passing through a bow shock, the wind material is supposed to fall down quasi-spherically to the magnetosphere of the neutron star (Davidson & Ostriker 1973). As a result, the line-of-sight direction traces a typical column density of the material around the neutron star. In contrast, if the material is accreted through a disk, most of the material is condensed into a disk, and the line-of-sight direction could trace a much less column density if the disk plane is not in the line-of-sight direction. Since similar fluxes between the spin-up period and the wind-fed state indicate similar mass accretion rates, the much less absorption column densities during the spin-up period support the scenario that the material is accreted through a disk-like structure, which spins up the neutron star.

The pulse profiles of GX 301-2 during the spin-up period show an interesting trend with luminosity: the main peak is similar to the faint peak during the slow spin-up period (with a luminosity $\sim 2 \times 10^{37} \text{ erg/s}$), but the main peak increases with the observed fluxes during the rapid spin-up period (with a luminosity $\sim 4 \times 10^{37} \text{ erg/s}$), while the faint peak keeps almost constant. Such a trend is confirmed by *Fermi*/GBM data at even higher luminosities ($\sim 8 \times 10^{37} \text{ erg/s}$). But the pulse profiles of wind-fed state show

no such a trend. These behaviors could be related to the emitting region/pattern at different luminosities.

For X-ray pulsars with low luminosity, the radiation is generally supposed to have a pencil beam due to anisotropic scattering cross-section of photons in a strong magnetic field. While above certain luminosity, an accretion column is formed, and the radiation is supposed to have a fan beam. The pulse profiles of GX 301-2 always showed a two-peaked feature from the lowest to the highest observed luminosities (e.g. La Barbera et al. 2005; Evangelista et al. 2010). The simplest appropriate model is to assume that each peak represents a pole, and each pole emits in a pencil beam (e.g. Wang & Welter 1981). The main peak corresponds to the pole close to the observer, while the faint peak corresponds to the further pole. If both poles produce a similar pencil-like beam, the observed increasing trend of the main peak with increasing luminosity indicates that the emission along the polar direction is increasing, while the little change of the faint peak indicates that the emission perpendicular to the polar direction is not changing much with increasing luminosity.

The pulse profiles of the neutron star could be related to luminosity in several different ways. The magnetosphere radius of an accreting neutron star depends on the B-field and luminosity as follows (e.g. Frank et al. 2002):

$$R_m = 2.8 \times 10^8 \Lambda B_{12}^{4/7} L_{37}^{-2/7} \text{ cm}, \quad (2)$$

where $\Lambda = 1$ for wind accretion and $\Lambda < 1$ for disk accretion, and we have adopted a neutron star mass of $1.5 M_\odot$ and radius of 10 km. The field line around the magnetosphere crosses the neutron star surface with an angle β relative to the magnetic axis:

$$\sin^2 \beta = \frac{R_{NS}}{R_m} \sin^2 \alpha, \quad (3)$$

where α is the angle between the disk plane and the magnetic axis. Therefore, the higher the luminosity, the larger the β . For wind accretion, the accreted material fills the whole column centered around the magnetic axis, and β is the radius of the column; while for disk accretion, the accreted material is confined to a narrow wall, which is away from the magnetic axis with an angle β (e.g. Basko & Sunyaev 1975, 1976). The changing direction of the hot spot with luminosity for disk accretion will affect the observed pulse profiles.

Another effect of different luminosities is radiation feedback. For X-ray pulsars with high luminosity, the accreted gas flow is decelerated by the radiation pressure, and a radiative shock is formed, below which the material is sinking down to the surface of neutron star (Basko & Sunyaev 1976). The critical luminosity depends on accretion process and the magnetic field, and is suggested to be around $1 \times 10^{37} \text{ ergs}^{-1}$ for a cyclotron energy around 30 keV, based on the bimodal variation of the cyclotron energy with luminosity (e.g. Becker et al. 2012; Mushtukov et al. 2015; Doroshenko et al. 2017). Therefore, it is possible that the emission pattern changes with luminosity around the observed luminosities. Sudden transitions of pulse profiles have been observed around $10^{38} \text{ ergs}^{-1}$ for several sources (e.g. Wilson-Hodge et al. 2018; Doroshenko et al. 2020), and the exact value of critical luminosity is not well understood. We emphasize that feedback of radiation is expected to alter

the geometry of the accretion disk/flow and such changes have indeed been observed (e.g. Wilson-Hodge et al. 2018; Doroshenko et al. 2020). Similar scenario could potentially apply also to GX 301-2.

On the other hand, the trend of only main peak changing with luminosity is not observed for wind state at luminosities around $4 - 8 \times 10^{37}$ ergs⁻¹. This could be due to the intrinsic differences between disk and wind accretion. As mentioned above, the filled column of wind accretion always lies along the magnetic axis, and only the radius of the column changes with luminosity, therefore, the inclination angle does not change with luminosity, different from disk accretion. At similar luminosity, the area of the hot spot of wind accretion is generally larger than that of disk accretion, and thus, the critical luminosity is different for disk and wind accretion (e.g. Mushtukov et al. 2015). This could lead to different emission pattern for disk and wind accretion at similar luminosity. We note that the above discussions assumed a simplified di-polar geometry of the magnetic field, and in reality, other effects, such as asymmetric magnetic field and gravitational light bending, could also play a role (e.g. Ftaclas et al. 1986; Bilous et al. 2019; Iwakiri et al. 2019). Detailed calculations of the pulse profile shapes for X-ray pulsars are required to reveal whether these processes can explain the observed different trend of pulse profiles for disk and wind accretion.

ACKNOWLEDGEMENTS

We thank our referee for his/her helpful suggestions. This work made use of data from the *Insight-HXMT* mission, a project funded by China National Space Administration (CNSA) and the Chinese Academy of Sciences (CAS), and also used data from *Fermi*/GBM and *Swift*/BAT. This work is supported by the National Key R&D Program of China (2016YFA0400800) and the National Natural Science Foundation of China under grants U1938113, 11773035, U1838201, U1938101, U1838202, 11473027, 11733009, U1838115, and is partially supported by the Scholar Program of Beijing Academy of Science and Technology (DZ BS202002). VD acknowledges support by the Russian Science Foundation (grant 19-12-00423).

DATA AVAILABILITY

The data underlying this article are publicly available at <http://archive.hxmt.cn>.

REFERENCES

- Abarr, Q. et al. 2020, *ApJ*, 891, 70
 Basko, M. M. & Sunyaev, R. A. 1975, *A&A*, 42, 311
 Basko, M. M. & Sunyaev, R. A. 1976, *MNRAS*, 175, 395
 Becker, P. A. et al. 2012, *A&A*, 544, 123
 Bildsten, L. et al. 1997, *ApJS*, 113, 367
 Bilous, A. V.; Watts, A. L.; Harding, A. K.; Riley, T. E.; Arzoumanian, Z.; Bogdanov, S.; Gendreau, K. C.; Ray, P. S. et al. 2019, *ApJ*, 887, 23
 Blondin, J. M. & Pope, T. C. 2009, *ApJ*, 700, 95
 Coburn, W.; Heindl, W. A.; Rothschild, R. E.; Gruber, D. E.; Kreykenbohm, I.; Wilms, J.; Kretschmar, P.; Staubert, R. 2002, *ApJ*, 580, 394
 Davidson, K. 1973, *NPhS*, 246, 1
 Davidson, K. & Ostriker, J. P. 1973, *ApJ*, 179, 585
 Doroshenko, V.; Santangelo, A.; Suleimanov, V.; Kreykenbohm, I.; Staubert, R.; Ferrigno, C.; Klochkov, D. 2010, *A&A*, 515, 10
 Doroshenko, V. et al. 2017, *MNRAS*, 466, 2143
 Doroshenko, V. et al. 2020, *MNRAS*, 491, 1857
 Evangelista, Y.; Feroci, M.; Costa, E.; Del Monte, E.; Donnarumma, I.; Lapshov, I.; Lazzarotto, F.; Pacciani, L. et al. 2010, *ApJ*, 708, 1663
 Finger, M. H. et al. 2009, arXiv0912.3847
 Frank, J., King, A., Raine, D. J. 2002, *Accretion Power in Astrophysics*, Cambridge Univ. Press, Cambridge
 Fryxell, B. A. & Taam, R. E. 1988, *ApJ*, 335, 862
 Ftaclas, C.; Kearney, M. W.; Pechenick, K. 1986, *ApJ*, 300, 203
 Fürst, F.; Falkner, S.; Marcu-Cheatham, D.; Grefenstette, B.; Tomsick, J. Pottschmidt, K.; Walton, D. J.; Natalucci, L.; Kretschmar, P. 2018, *A&A*, 620, 153
 Ghosh, P. & Lamb, F. K. 1979, *ApJ*, 234, 296
 Iwakiri, W. B.; Pottschmidt, K.; Falkner, S.; Hemphill, P. B.; Fürst, F.; Nishimura, O.; Schwarm, F. W.; Wolff, M. T. et al. 2019, *ApJ*, 878, 121
 Kaper, L.; van der Meer, A.; Najjarro, F. 2006, *A&A*, 457, 595
 Kreykenbohm, I. et al. 2004, *A&A*, 427, 975
 Koh, D. T.; Bildsten, L.; Chakrabarty, D. 1997, *ApJ*, 479, 933
 La Barbera A., Segreto A., Santangelo A., Kreykenbohm I., Orlandini M., 2005, *A&A*, 438, 617
 Lamb, F. K., Pethick, C. J., Pines, D. 1973, *ApJ*, 184, 271
 Leahy, D. A. & Kostka, M. 2008, *MNRAS*, 384, 747
 Liao, Jin-Yuan; Zhang, Shu; Chen, Yong; Zhang, Juan; Jin, Jing; Chang, Zhi; Chen, Yu-Peng; Ge, Ming-Yu et al. 2020, *JHEAp*, 27, 24
 Liu, J. 2020, *MNRAS*, 496, 3991
 Mönkkönen, J., Doroshenko, V., Tsygankov, S. S., Nabizadeh, A., Abolmasov, P., Poutanen, J. 2020, *MNRAS*, 494.2178
 Makishima, K. et al. 1988, *Nature*, 333, 746
 Malacaria, C., Jenke, P., Roberts, O. J., Wilson-Hodge, C. A., Cleveland, W. H., Mailyan, B. 2020, arXiv:2004.00051
 Meegan, C. et al. 2009, *ApJ*, 702, 791
 Mushtukov, A. A.; Suleimanov, V. F.; Tsygankov, S. S.; Poutanen, J. 2015, *MNRAS*, 447, 1847
 Nabizadeh, A.; Mönkkönen, J.; Tsygankov, S. S.; Doroshenko, V.; Molkov, S. V.; Poutanen, J. 2019, *A&A*, 629, 101
 Pravdo, S. H.; Ghosh, P. 2001, *ApJ*, 554, 383
 Pringle, J. E.; Rees, M. J. 1972, *A&A*, 21, 1
 Rappaport, S. & Joss, P. C. 1977, *Nature*, 266, 683
 Sato, N.; Nagase, F.; Kawai, N.; Kelley, R. L.; Rappaport, S.; White, N. E. 1986, *ApJ*, 304, 241
 Schonherr et al. 2007, *A&A*, 472, 353
 Sepinsky, J. F., Willems, B., Kalogera, V. 2007, *ApJ*, 660, 1624
 Wang, Y. M. & Welter, G. L. 1981, *A&A*, 102, 97
 White, N. E.; Mason, K. O.; Huckle, H. E.; Charles, P. A.; Sanford, P. W. 1976, *ApJ*, 209, L119

Wilms, J.; Allen, A.; McCray, R. 2000, ApJ, 542, 914
Wilson-Hodge, C. A. et al. 2018, ApJ, 863, 9
Xu, W. & Stone, J. M. 2019, MNRAS, 488, 5162
Zhang, S. N. et al. 2020, SCPMA, 63, 9502